Remote Sensing of Environment 215 (2018) 228–241

Contents lists available at ScienceDirect

Remote Sensing of Environment

journal homepage: www.elsevier.com/locate/rse

On the determination of global ocean wind and wave climate from satellite observations

I.R. Young[a,*], M.A. Donelan[b]

[a] Department of Infrastructure Engineering, The University of Melbourne, Vic 3010, Australia
[b] Rosenstiel School of Marine and Atmospheric Science, University of Miami, Miami, FL, USA

A B S T R A C T

Three extensive global wind speed and wave height datasets (altimeter, radiometer, model reanalysis) are analysed to investigate the global wind speed and wave height climate. Despite the fact that these datasets have all been carefully calibrated, they show systematic differences in wind speed. At high latitudes both altimeter and radiometer winds are biased high compared to buoy measurements. Altimeter winds are more impacted than radiometer winds. Based on the assumptions that altimeter winds respond primarily to the surface wave spectrum mean squared slope and radiometer winds respond primarily to the surface wave spectrum dissipation, it is shown that the observed differences are a result of changes in atmospheric stability. An analysis which accounts for differences in air and water temperatures describes the observed differences with surprising accuracy. Based on this analysis corrections to both altimeter and radiometer winds are proposed which account for the influence of atmospheric stability. It is also shown that satellites preferentially measure at particular local times of day. As winds have a diurnal variation in magnitude, this preferential measurement time can also bias statistical values obtained from such satellite systems.

1. Introduction

Long term global datasets of satellite observations of wind speed and wave height provide a potentially valuable resource to study global climatology and changes in climate. To realize this value, however, such datasets need to be carefully calibrated and validated. Such studies need to validate satellite observations against “ground truth” under a variety of meteorological conditions and across a broad range of geographic locations. In the case of wind speed and wave height measurement from satellites there are a number of issues that challenge our ability to meet all these desired validation criteria. “Ground truth” for such instruments are generally measurements from floating buoys. Such buoys have a limited geographic distribution, limiting our ability to validate under all possible conditions. In addition, there are questions about how well such instruments measure these quantities. Do floating buoys accurately follow the water surface for the measurement of wave height? Can anemometer measurements made relatively close to the water surface (e.g. 4 m) be accurately scaled up to a reference height of 10 m.

In addition, oceanographic satellites do not measure either wind speed or wave height directly. Rather, they measure properties of the water surface, which can then be related to either wind speed or wave height. As a result, questions exist about the veracity of relationships relating the sensed quantities to wind speed and wave height under all possible conditions.

This study examines the large and extensively calibrated and validated satellite altimeter and radiometer dataset of Young et al. (2017) to investigate global wind and wave climate. The satellite dataset is complemented with the model reanalysis dataset ERA-Interim. Based on comparative analysis of this climatology, consistent differences in wind speed measurements between altimeters and radiometers are detected. These differences are shown to be the result of changes in the structure of the atmospheric boundary layer due to differences in atmospheric stability (air-water temperature difference). Relationships which can correct both altimeter and radiometer wind speed measurements are developed to take account of these atmospheric stability effects.

The arrangement of the paper is as follows. Following this Introduction, Section 2 describes the three datasets used in the analysis – altimeter, radiometer, ERA-Interim. Section 3 discusses a range of issues associated with the measurement of wind speed from satellites. Section 4 presents results from the various datasets of global wind speed and wave height climate followed by an analysis of wave age and atmospheric stability effects in Section 5, as possible explanations of

* Corresponding author.
E-mail address: ian.young@unimelb.edu.au (I.R. Young).

https://doi.org/10.1016/j.rse.2018.06.006
Received 5 March 2018; Received in revised form 2 June 2018; Accepted 5 June 2018
0034-4257/

differences between the satellite platforms, in the observed climatology. A discussion of the results is presented in Section 6 followed by Conclusions.

2. Datasets

Three long-duration datasets have been used in this analysis; the altimeter and radiometer datasets reported by Young et al. (2017) and the reanalysis numerical model dataset ERA-Interim (Dee et al., 2011).

2.1. Radar altimeters

The Radar altimeter missions included in the present database (in order of launch) are: GEOSAT, ERS1, TOPEX, ERS2, GFO, JASON1, ENVISAT, JASON2 and CRYOSAT. These missions cover the period from 1984 to 2014 (see Young et al., 2017). The altimeter (ALT) is an active instrument, transmitting radar pulses which are averaged to provide measurements of significant wave height, H_s and wind speed (at 10 m height and averaged over 10 min), U_{10}. The footprint of the ALT varies between 8 km and 10 km and data is provided approximately every 1 s (approx. 10 km) along the satellite track. The ALT missions were placed in a variety of near-polar orbits. Depending on the details of the orbit, the satellite will re-trace its ground tracks after a period between 5 and 20 days. This duration is termed an Exact Repeat Mission (ERM). The ERM defines the ground track separation, with a long ERM corresponding to a relatively small ground track separation. The ground track separation decreases with increasing latitude. At the Equator, values range between 100 km and 400 km. Thus, the ALT has relatively high resolution along track (10 km) and low resolution across track (100 km to 400 km). This low cross-track resolution together with the long ERM, means that, although the ALT provides global coverage, it is possible that storms may be under-sampled or completely missed.

As noted above, the ALT missions were all in near-polar orbits. Fig. (1) shows a histogram of the number of ALT passes through two 2° × 2° regions as a function of the local time of day [Fig. (1a) centred on 56°N, 180°E and Fig. (1b) centred on 0°, 10°E]. As can be seen in these figures, the time of day of the satellite overflight is not uniformly distributed. This is because ERS1, ERS2 and ENVISAT were in "sun-synchronous" orbits, where every time the satellite crosses the equator, it is at the same local time. This explains the spikes which occur at approximately 10 h and 22 h, associated with ascending and descending passes, respectively. Therefore, although the combined ALT missions provide global spatial coverage, the temporal coverage at given locations are concentrated at these specific times of day. These preferential local times of satellite overflight will be approximately the same for all locations. If the geophysical quantities measured by the ALT vary on a diurnal basis, this may introduce a bias in the measured quantities (e.g. diurnal variations in wind speed).

Based on the shape and intensity of the returned radar signal from the footprint, the ALT can estimate the significant wave height H_s and wind speed U_{10} (Cheney et al., 1987; Walker, 1995; Chelton et al., 2001; Queffeulou, 2004; Young, 1994, 1999a, 1999b; Zieger et al., 2009).

The significant wave height, H_s can be determined from the slope of the leading edge of the radar return (Chelton et al., 2001; Holthuijsen, 2007). This is based on the assumption that a calm sea would act like a mirror and the return pulse would approximate a "square wave" (i.e. near vertical leading edge to the return signal), whereas a "wavy" surface will result in a leading edge, the slope of which decreases with increasing H_s.

The wind speed, U_{10} is determined from the ratio of the intensity of the incident to the reflected radar energy (radar cross-section, σ_0) (Chelton et al., 2001). The relationship between U_{10} and σ_0 is nonlinear, with σ_0 decreasing as U_{10} increases. The assumption is that the high wavenumber components of the surface wave spectrum respond almost immediately to the local wind, and that these relatively steep, short wavelength components act as scatters, increasingly scattering radar energy as U_{10} increases. The exact quantity related to the high wavenumber spectrum upon which U_{10} depends is not known, although it is reasonable to assume that the slope of the high wavenumber components plays an important role. Hwang et al. (1998) and Plant (2002) provide a detailed analysis showing that the ALT responds to surface tilting slopes approximately 3 to 5 times longer than the electromagnetic radiation.

In practice, both H_s and U_{10} are determined by empirical calibration based on buoy data (e.g. Abdalla, 2007; Cotton and Carter, 1994; Young, 1993, 1999a, 1999b; Zieger et al., 2009). In the case of U_{10} this adds the additional issue of relating buoy measurements at an anemometer height which is usually less than 10 m to this reference height. This is usually achieved assuming a neutral logarithmic boundary layer (see Section 3). Therefore, ALT H_s is obtained from a direct relationship – the slope of the leading edge of the return pulse is directly related to H_s. In contrast, ALT U_{10} is determined indirectly – the near surface wind generates high wavenumber components of the spectrum which scatter the radar energy, the amount of scattering is then related to the wind speed at a height of 10 m, scaled from buoy data assuming a specific boundary layer shape (see Section 3).

2.2. Radiometers

The radiometer (RAD) missions included in the present study were: SSMI f08, f10, f11, f13, f14, f15, f16, f17, AMSRE, TMI and WINDSAT.

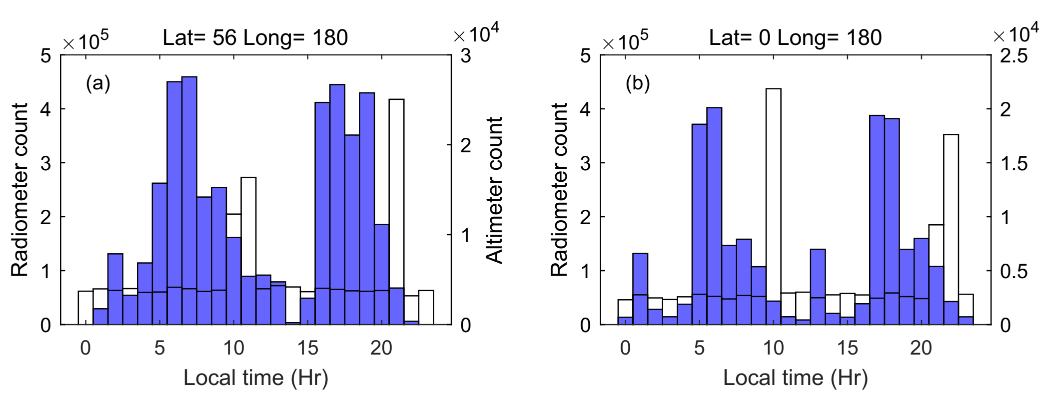

Fig. 1. Histogram of the number of satellite observations in two 2° × 2° squares for the full durations of the satellite datasets as a function of the local hour of the day. RAD values solid blue bars (left axis), ALT values open bars (right axis). (For interpretation of the references to colour in this figure legend, the reader is referred to the web version of this article.)

These missions cover the period 1987 to 2014, similar to the ALT missions (see Young et al., 2017). The RAD is a passive instrument, measuring the emissivity of the ocean surface at a number of frequencies, this quantity being characterised by the brightness temperature, T_B. With the exception, of TMI, which has an orbit limited by latitudes $\pm 40^\circ$, the other RAD missions were placed in sun-synchronous, near-polar orbits. In contrast to the ALT, the RAD measures over a broad swath of approximately 1400 km width. The resolution of the measurements within the swatch is 25 km (both across and along track). As such, a single RAD mission will image almost the full globe twice per day. Fig. (1) shows histograms of the local time of RAD passes for the same two $2^\circ \times 2^\circ$ regions, as for the ALT missions. The local crossing times of the RAD sun-synchronous orbits vary between missions and a number drifted over time. As a result, there is a span of local crossing times shown in Fig. (1). Nevertheless, the histogram does peak at local crossing times of 6 h and 18 h, approximately 4 h earlier than the ALT missions. Therefore, as for the ALT, the RAD provides global coverage but with observations not uniformly distributed diurnally. As these preferential crossing times are not the same as the ALT, this may result in differences in quantities measured by the two satellite systems.

Wentz (1983, 1992, 1997) showed that there is a relationship between the brightness temperature, T_B and the three geophysical quantities: near surface wind speed, U (ms^{-1}), columnar water vapour, V (mm) and columnar cloud liquid water, L (mm). The relationship between these quantities is defined by a radiative transfer equation, which has been expressed by Wentz (1983) in a closed form. As the radiometer measures at a number of frequencies, there is sufficient data to solve the radiative transfer equation for each of these quantities. Although the primary dependence of T_B is on the three parameters above, there is also a secondary dependence on: sea-surface temperature, T_s (°K), effective atmospheric temperature, T_E (°K), effective atmospheric pressure P (hPa) of the water column and the wind direction, ϕ. The first three of these quantities are determined from climatological values and ϕ is included as a fourth quantity to be obtained in the solution of the radiative transfer equation. As with ALT data, the model is calibrated against buoy data (Wentz, 1997). It should be noted that the signal is degraded during rain events and hence the above analysis is strictly applicable in non-rain conditions.

In the present study, RAD data is used to measure global values of U_{10}. As with the ALT, the RAD does not measure U_{10} directly, rather it is through the effect that the near-surface wind has on the emissivity of the water surface. It has been shown that the emissivity is related to the ocean surface roughness (high wavenumber components of the surface wave spectrum) (Wentz, 1992). It has also been shown that there are three primary processes responsible for this dependence. Firstly, surface wave components longer than the radiating wavelength will mix the horizontal and vertical polarization states and change the local incidence angle. Secondly, sea foam associated with wave breaking (including micro-breaking of high wavenumber components) (Stogryn, 1972) influence the radiation from the surface. Thirdly, there is an impact from the diffraction of microwaves by surface waves that are small compared to the radiation wavelength. A host of studies have considered these quantities and their relative importance (Yueh et al., 1994; Johnson and Zhang, 1999; Hwang, 2012; Hwang and Fois, 2015; Meissner et al., 2014, 2017). As for ALT, these mechanisms are not used directly in the solution process, rather the radiative transfer model is calibrated against buoy data for wind speed, parameterised at a height of 10 m based on the assumption of a neutral stability logarithmic boundary layer.

2.3. ERA-Interim Reanalysis data

ERA-Interim (ERA-I) is a global atmospheric reanalysis from 1979 (Dee et al., 2011). In the present study, data has been used for the period from 1984 to 2014, to correspond to the approximate period of the satellite datasets. ERA-I uses the ECMWF Cy31r2 atmospheric model coupled with the WAM spectral wave model (Komen et al., 1994; Janssen, 2008). Both the atmospheric model and the wave model used in ERA-I incorporate satellite data assimilation. The radiances from the radiometers were used by ERA-I (not U_{10}) and the significant wave heights from the altimeters. As such, some of the satellite data outlined above will have been assimilated into this reanalysis dataset. The model data is supplied to uses at a spatial resolution of 0.75° with data archived at 6 hourly intervals. The atmospheric data, however, have a native grid resolution of the order of 80 km, whereas for the wave data, the native grid resolution is 111 km. A variety of ERA-I geophysical quantities have been used in the present study: wind speed at 10 m, U_{10}, significant wave height, H_s, mean wave period, T_m, air temperature at an elevation of 2 m, T_2 and sea surface temperature, T_s. With the exception of T_s, these quantities are all produced by the coupled model system. The sea surface temperature is a specified boundary condition for the atmospheric model. ERA-Interim used a succession of different T_s data sources (Dee et al., 2011; Kumar et al., 2013).

3. Wind speed measurements from satellites

As noted in Section 2, both ALT and RAD measure wind speed indirectly. In the case of both systems, they measure quantities associated with the high wavenumber components of the surface wave spectrum. It is assumed that these quantities are related to the near surface wind speed. Neither the precise definition of the near surface wind speed (i.e. at what height) nor the surface wave spectral quantity (i.e. mean squared slope, surface stress, surface wave dissipation) are defined. Rather, the quantities measured by the satellite system (ALT – radar cross-section; RAD – brightness temperature) are related to the wind speed at a height of 10 m, U_{10}, through model calibration against buoy measurements. This process overcomes the need to understand just what process is causing the relationship between the imaged quantity of the surface wave spectrum and wind speed. However, it requires that the structure of the atmospheric boundary layer when a measurement is made is similar to that for the calibration.

The buoy data is seldom measured at an anemometer height of 10 m and is typically extrapolated to this height assuming a neutral stability logarithmic boundary layer. The atmospheric boundary layer can be represented by (e.g. Priestly, 1959; Lumley and Panofsky, 1964; Webb, 1970)

$$\frac{u(z)}{u_*} = \frac{1}{\kappa}\left[\ln\left(\frac{z}{z_0}\right) - \psi(z/L_0)\right] \tag{1}$$

where, $u(z)$ is the wind speed as a function of elevation, z, $u_* = \sqrt{C_d}\,U_{10}$ is the friction velocity and C_d is the drag coefficient, z_0 is the surface roughness height and ψ is called the integrated universal function and is based on the Monin-Obukhov formalism (Monin and Obukhov, 1954; Monin and Yaglom, 1971). The quantity, L_0 is the Obukhov scale length (Arya, 1988), given by

$$L_0 = \begin{cases} z/10.1R_b & \text{for } R_b < 0 \\ z/8R_b & \text{for } R_b \geq 0 \end{cases} \tag{2}$$

where R_b is the bulk Richardson number, given by (Kahma and Calkoen, 1992)

$$R_b = \frac{gz(T_z - T_s)}{T_z U_z} \tag{3}$$

and T_z is the air temperature at height z, T_s is the sea surface temperature and U_z is the wind velocity at height z. The integrated universal function, ψ is given by (Webb, 1970; Dyer and Hicks, 1970; Businger et al., 1971)

$$\psi = \begin{cases} 2\ln\left(\frac{1+x}{2}\right) + \ln\left(\frac{1+x^2}{2}\right) - 2\tan^{-1}x + \pi/2 & \text{for } L_0 < 0 \\ -\frac{5z}{L_0} & \text{for } L_0 \geq 0 \end{cases} \tag{4}$$

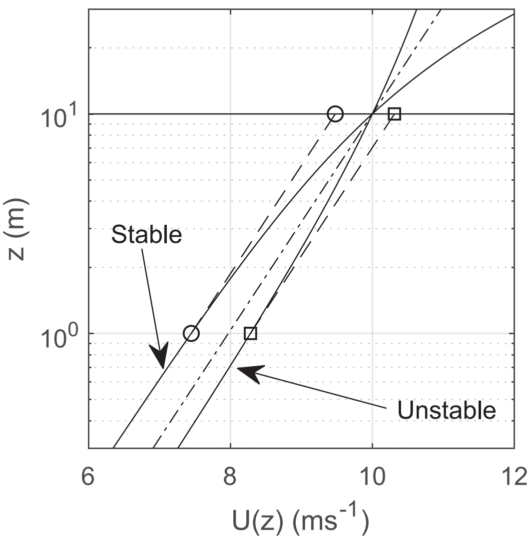

Fig. 2. Atmospheric boundary layer for three cases: stable and unstable (marked) and neutral (dash-dot line). The boundary layers are calculated from Eq. (1). The dashed lines show the potential error if values are extrapolated to a height of 10 m assuming a neutral boundary layer.

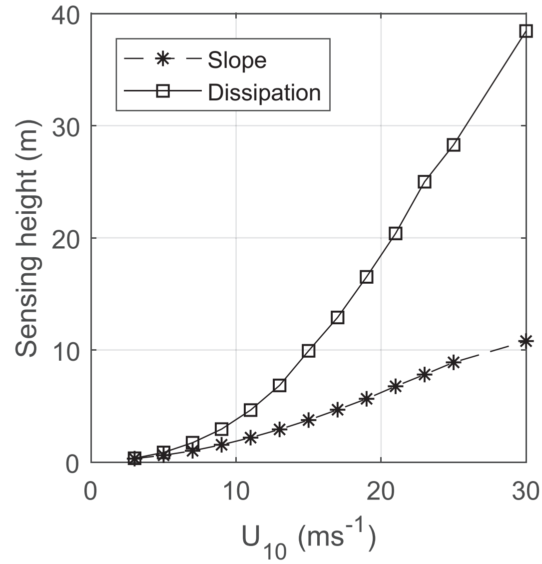

Fig. 3. Effective sensed height of the wind speed, assuming the quantity impacting the surface wave spectrum is: mean squared slope (*), dissipation, (□).

where $x = (1 - 16z/L_0)^{1/4}$.

A typical application of Eqs. (1) to (4) is shown in Fig. 2. In the case shown, $T_s = 20^{\circ}$C and the air temperature T_{10} is 15°C (unstable conditions) and 25°C (stable conditions). When the water is warmer than the air there is an upward flux of heat and an atmospheric density gradient with denser air overlaying less dense air (L_0 is negative). Such an unstable boundary layer results in a more uniform distribution of wind speed through the boundary layer than a neutral condition ($\frac{1}{L_0} \cong 0$). The converse occurs when the water is cooler than the air (stable boundary layer). The resulting boundary layer distributions are shown in Fig. (2).

The three cases shown in Fig. 2 all have $U_{10} = 10\ \mathrm{ms}^{-1}$, however, different wind speeds at a height close to the water surface (in this case an example height of 1 m has been chosen). If these near surface wind speeds were extrapolated to a height of 10 m assuming a neutral boundary layer, it would result in an overestimation for an unstable boundary layer and an underestimation for a stable boundary layer. Thus, the satellite system (ALT or RAD), which actually responds to a near surface wind speed, will over/under estimate in unstable/stable boundary layer conditions. The sensitivity to boundary layer stability will vary according to the effective height of the wind sensed by the satellite. Therefore, a system which responds to the very high wavenumber components of the spectrum and therefore an effective wind at a low height will be more sensitive to stability than a system which responds to lower wavenumber surface wave spectrum components.

As noted above, radar altimeters provide, to first order, a measure of the inverse mean square slope of the surface (mss) (other quantities may also influence the altimeter return but are assumed secondary in this analysis). Since mss and wind speed are closely correlated (Cox and Munk, 1954; Munk, 2009; Donelan, 2018), satellite altimeters function as anemometers and are calibrated against U_{10} from buoys. The underlying assumption is that the radar cross-section (mss) is related to the wind speed at 10 m height regardless of the magnitude of the wind speed. This is clearly not so, as light winds generate relatively short wavelengths while strong winds generate longer wavelengths, which interact with the wind at widely different heights. To assess the effective height of the wind generating the mss, we note that the energy input to the waves can be associated with the wind at one half wavelength, $U_{\lambda/2}$, height (Yang et al., 2013; Donelan, 2018). The effective height, z_{mss}, is the weighted mean of the $\lambda_i/2$ weighted by the slope squared contribution from each wavelength (the i subscript signifying a range of components of the spectrum).

$$z_{mss} = \frac{\int_0^{k_{top}} F(k)k^2\lambda(k)/2dk}{\int_0^{k_{top}} F(k)k^2dk} \tag{5}$$

where $F(k)$ is the wave number spectrum, and $k_{top} = 10^3\ \mathrm{m}^{-1}$, is an arbitrarily chosen high value.

The slope squared contributions are predominantly from the short waves and, in fact, are significant even out to capillary waves of 6 mm wavelength. We have applied the wideband wave prediction model of Donelan (2018) to determine the spectrum in Eq. (5). This model was run for a range of wind speeds and integrated out to long fetch to produce representative spectra for open ocean conditions. The resulting values of z_{mss} are shown in Fig. 3 for a range of wind speeds. As can be seen in the figure, as the wind speed increases, the scale of the waves generated by the wind increases and the weighted mean height of the wind generating the mss increases. As a result, the effective height of the wind speed sensed by the altimeter increases with wind speed.

Radiometers estimate the wind speed from the brightness temperature, which, as noted above, is related to the degree of whitecapping or the integrated dissipation rate of the waves across the spectrum (Donelan, 2018). Again, as noted above, other quantities also influence the brightness temperature, however, as shown later in this paper, dissipation rate seems to account for most of the observed structure reported here. Donelan et al. (2012) and Donelan (2018) propose a dissipation source term, S_{ds} of the form

$$S_{ds}(k) = -A_2[1 + A_3\chi(k)^2]^2B(k)^{2.53}\omega(k)F(k) \tag{6}$$

where $\chi(k)^2$ is the mean squared slope of all wave components longer than $\lambda(k)$, $\omega = \sqrt{gk}$ is the frequency of spectral components and $A_2 = 46.665$ and $A_3 = 240$ (Donelan, 2018). The omni-directional saturation spectrum $B(k) = F(k)k^3$. Similar to Eq. (5), the effective dissipation height, z_{diss} is given by the weighted integral

$$z_{diss} = \frac{\int_0^{k_{top}} S_{ds}(k)\lambda(k)/2dk}{\int_0^{k_{top}} S_{ds}(k)dk} \tag{7}$$

The dissipation rate is more evenly distributed across the spectrum

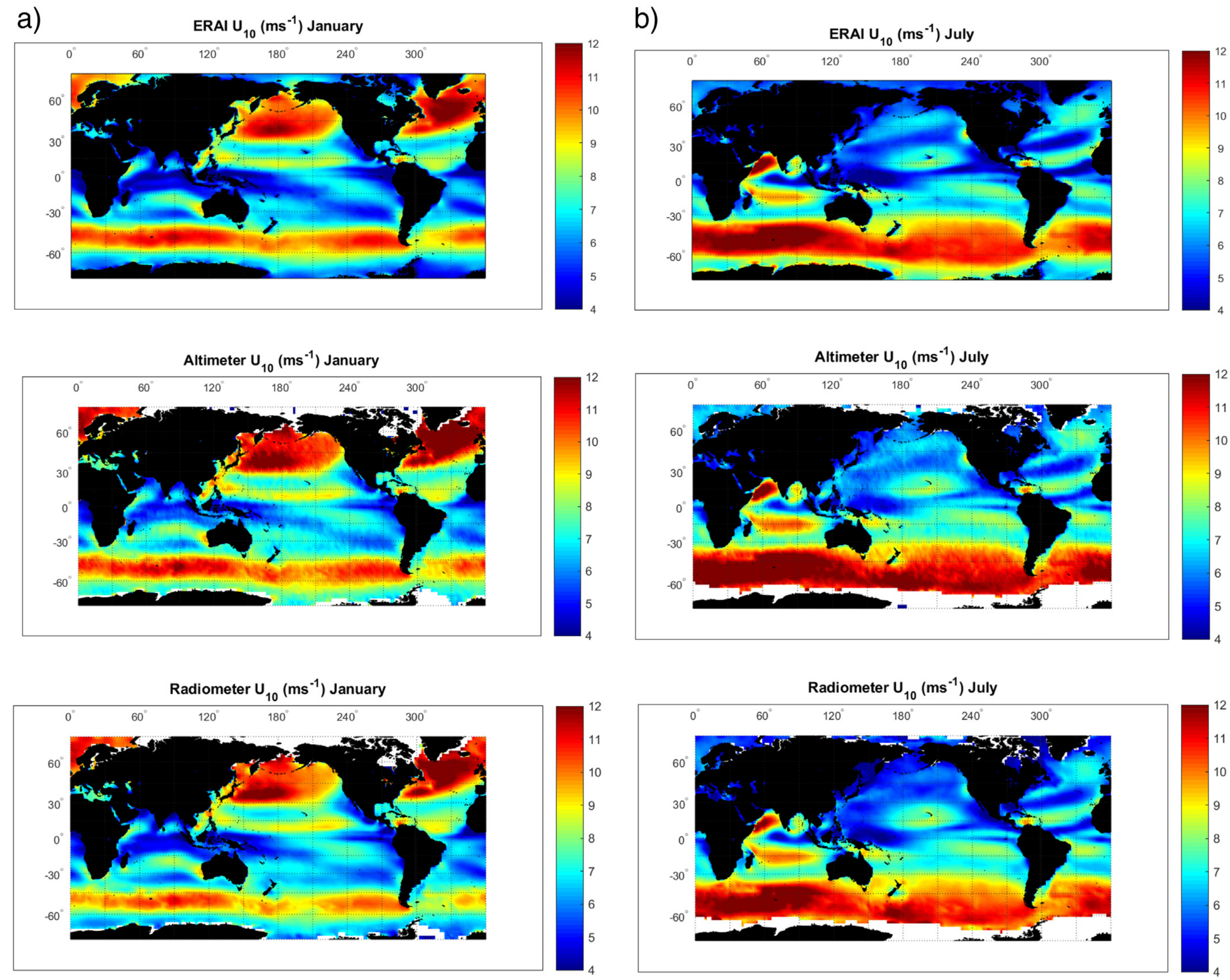

Fig. 4. (a) Mean monthly wind speed, U_{10} (ms^{-1}) for January. ERA-I (top), ALT (middle), RAD (bottom). (b) Mean monthly wind speed, U_{10} (ms^{-1}) for July. ERA-I (top), ALT (middle), RAD (bottom).

than the mss, and so the weighted effective heights are considerably greater, as shown in Fig. 3. As a result, for the same wind speed, the effective wind speed height sensed by the radiometer ('dissipation') is higher than the altimeter ('mss'). Evaluating the integrals in Eqs. (5) and (7) to C-band wavenumbers ($k_{top} = 110\,\mathrm{m}^{-1}$), rather than the assumed $k_{top} = 10^3\,\mathrm{m}^{-1}$ makes imperceptible differences in z_{mss} and even less in z_{diss}.

4. Global climatology

The raw ALT and RAD datasets were processed using the calibration relationships proposed by Young et al. (2017). The data was then binned into 2° × 2° bins and mean monthly values calculated for each bin. The ERA-I data was available on an 0.75° × 0.75° grid and this grid was utilized, again with mean monthly values being calculated for each grid point. Fig. (4a) and (b) show the mean month wind speed (U_{10}) for January [Fig. (4a)] and July [Fig. (4b)] for each of ERA-I, ALT and RAD. Fig. (5a) and (b) show mean monthly significant wave height (H_s) for January [Fig. (5a)] and July [Fig. (5b)] for each of ERA-I and ALT (i.e. RAD does not measure wave height).

Global climatologies of wind speed and wave height have been produced previously (Young, 1994, 1999a, 1999b; Young and Holland, 1996), however, the results in Figs. 4 and 5 are unique in that they are obtained from both model and satellite and from different satellite systems. This provides the opportunity for a comparative analysis of the results.

The similarity of results across the three data sources is remarkable (two sources for wave height). Although both ALT and RAD have been compiled on the same 2° × 2° grid, the lower spatial resolution of the ALT is clear in the figures (see also Fig. 1). Nevertheless, both qualitative and quantitative features are consistent across all data sources. Both wind speed and wave height show a clear seasonal cycle with high wind speed and wave height being seen at high latitudes in the respective winters. The summer-winter cycle is much stronger in the Northern Hemisphere than in the Southern Hemisphere. Although the maximum values in both hemispheres are comparable during their respective winters, the Southern Hemisphere still exhibits quite high wind speeds and wave heights in summer. In contrast, Northern Hemisphere summers are relatively calm with values comparable to Equatorial values.

The wind speed distributions (Fig. 4) show strong zonal features such as trade wind belts which are remarkably consistent across all data sources. In contrast, the spatial distributions of wave height are much more uniform without the detailed spatial variations seen in wind speed. This occurs because of the dispersive nature of waves, which effectively acts as an integrator receiving energy from the wind over

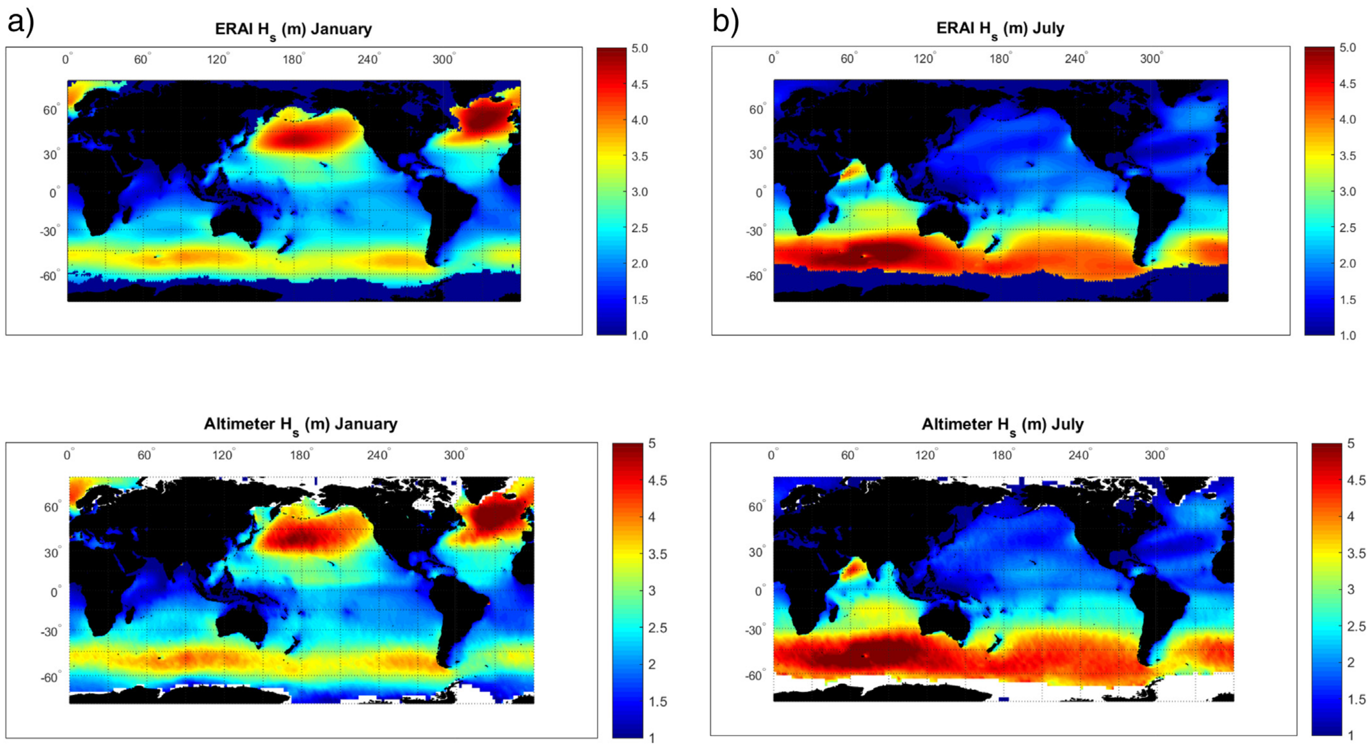

Fig. 5. (a) Mean monthly significant wave height, H_s (m) for January. ERA-I (top), ALT (bottom).
(b) Mean monthly significant wave height, H_s (m) for July. ERA-I (top), ALT (bottom).

extended fetch and then propagating across oceanic basins as swell. As a result, the spatial distributions are far more uniform than for wind speed.

Another clear feature is the “west coast wave climates” in the Southern Hemisphere. All the major continents (Africa, Australia, South America) exhibit higher wave heights year-round on their west coasts compared to their respective east coasts. A clear wave shadow also exists east of New Zealand (downwind). In contrast there is little difference in wind speed east and west of these continents. Clearly, these features are caused by the predominately west to east propagation of swell and the reduced fetches which exist east of each of these land masses.

The global distributions of wind speed for ALT and RAD are similar — noting that there is typically 20 times more data per grid square for the RAD than the ALT [see Section 2 and Fig. (1)]. It appears that at high latitudes the ALT gives slightly higher values than the RAD. This is more clearly seen in Fig. (6a) and (b) which show $\Delta U_{10} = U_{10}(ALT) - U_{10}(RAD)$. Fig. (6a) shows the difference for January and Fig. (6b) for July. The values in Fig. (6) are in physical units (ms^{-1}) and hence it may be assumed that the differences simply reflect the case that the winds are stronger at high latitudes. However, essentially the same result is achieved if the plots are presented in percentage terms. Also, Fig. (6b) shows a large difference in the northern hemisphere summer (July) when the mean wind speeds are relatively low and comparable to equatorial values [see Fig. (4b)].

Such a difference is surprising since the two satellite systems have both been calibrated against the same extensive buoy network (Young et al., 2017). As such, one would not expect the differences apparent in these results. It should be noted however, Young et al. (2017) calibrated the satellite systems against all the data from the NDBC buoy network. The majority of these buoys are at latitudes less than 45°N. That is, in regions where the differences in Fig. (6) are relatively small.

To understand buoy-satellite system differences in more detail, the Young et al. (2017) datasets were used to investigate the difference $\Delta U_{10} = U_{10}(\text{Sat}) - U_{10}(\text{buoy})$, where $U_{10}(\text{Sat})$ is the calibrated wind speed measured by the satellite (either ALT or RAD) and $U_{10}(\text{buoy})$ is the corresponding wind speed from the buoy, adjusted to 10 m assuming a neutral boundary layer. Each value satisfied the spatial and temporal matchup criteria of Young et al. (2017) (50 km and 30 min). The results for each of the satellite systems were determined as a function of time and monthly averages calculated.

The seasonal variations in ΔU_{10} are shown in Fig. (7) for two RAD and two ALT missions [SSMIf13 – Fig. (7a), SSMIf15 – Fig. (7b), ENVISAT – Fig. (7c), JASON1 – Fig. (7d)]. In order to investigate the variation with latitude, the values of ΔU_{10} are partitioned by latitude. Values were grouped for buoys between 0° and 30°N, 30°N and 50°N, greater than 50°N. Note that no significant Southern Hemisphere buoy data is available.

It is clear that as latitude increases ΔU_{10} also increases (satellite U_{10} is greater than buoy). This trend is stronger for the ALT than the RAD. Also, there is a clear seasonal signal, for both ALT and RAD with an overestimate (compared to buoys) of U_{10} in winter and a slight underestimate in summer. To investigate whether the seasonal signal in ΔU_{10} is simply due to the larger wind speeds in winter, the same analysis was conducted for H_s. Fig. (8) shows $\Delta H_s = H_s(\text{Alt}) - H_s(\text{buoy})$, partitioned by latitude, as a function of month. As in Fig. (7), the altimeters ENVISAT – Fig. (8a) and JASON1 – Fig. (8b) are considered (radiometers do not measure wave height). In stark contrast to wind speed, ΔH_s is approximately zero, with no variation with latitude or season. Hence, the features seen in Figs. (6) and (7) appear to be associated with wind speed measurements and not wave height.

An alternative way to examine the relative dependence with latitude of both RAD and ALT is to carry out a linear regression analysis between the satellite derived wind speed/wave height and the buoy. Again, the matchup data were partitioned by latitude as in Figs. (7) and (8). The resulting regression relations were then evaluated at the approximately mean global values ($U_{10} = 7.5\ \text{ms}^{-1}$ and $H_s = 2.0$ m). These values were then normalized by the regression value for the entire matchup dataset. Therefore, a value of 1.0 indicates that the data is identical to the total dataset average. A value of, for example 1.05,

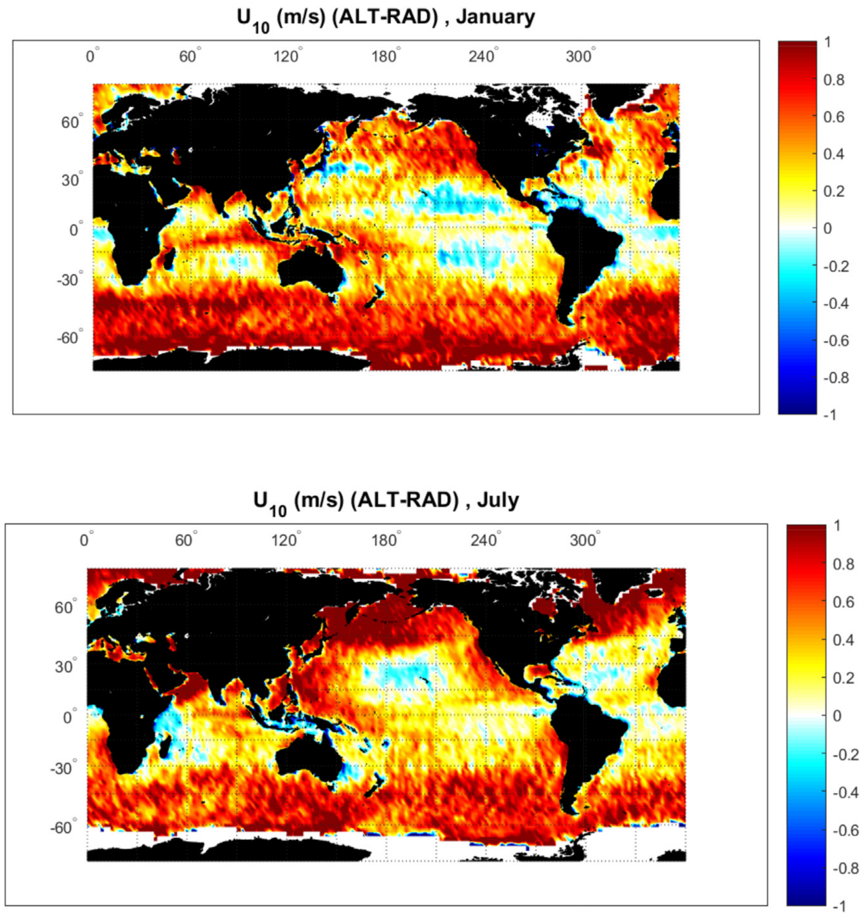

Fig. 6. Wind speed difference (U_{10}(ALT) − U_{10}(RAD)) (ms^{-1}) for January (top) and July (bottom). Positive values indicate ALT larger than RAD.

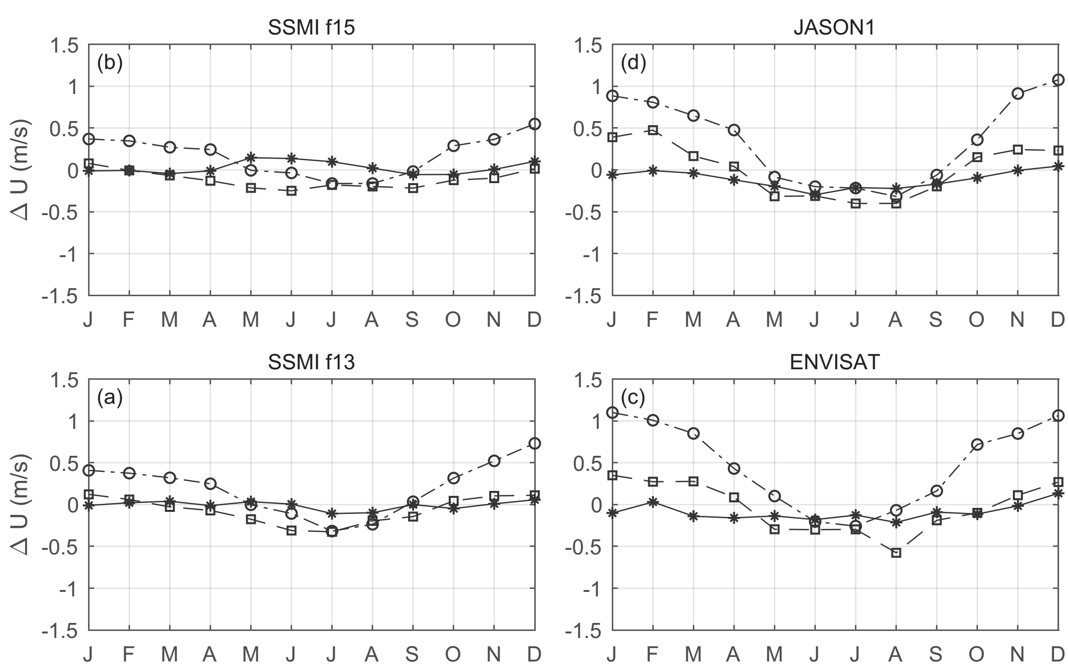

Fig. 7. Wind speed difference U_{10}(Sat) − U_{10}(buoy) as a function of month. Data partitioned by latitude: 0° to 30°N – (*), 30°N to 50°N – (□), greater than 50°N – (o). Radiometers SSMIf13 and SSMIf15 [panels (a) and (b)], Altimeters ENVISAT and JASON1 [panels (c) and (d)].

indicates that the satellite overestimates at that latitude, compared to the overall average by 5%.

Fig. (9) shows this analysis for both U_{10} and H_s and for each of the satellite missions in the full dataset. In addition to the mean regression values, the 95% confidence limits are shown. The confidence limits increase for latitudes above 50°N, as the number of buoy observations is

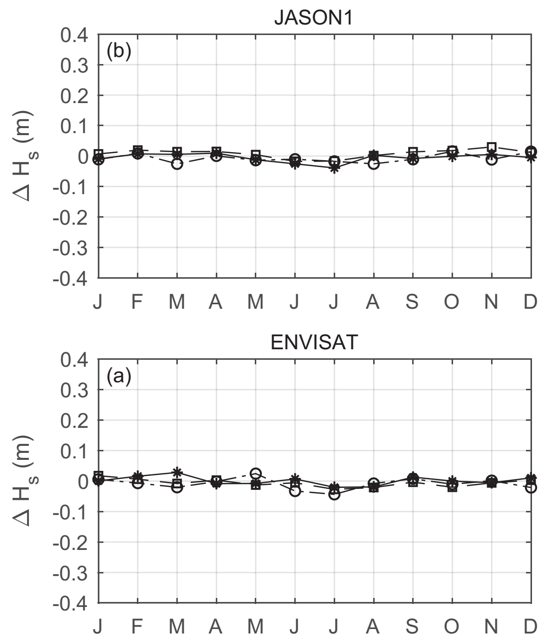

Fig. 8. Significant wave height difference H_s(Sat) − H_s(buoy) as a function of month. Data partitioned by latitude: 0° to 30°N – (*), 30°N to 50°N – (□), greater than 50°N – (o). Altimeters ENVISAT and JASON1 [panels (a) and (b)].

relatively small at these latitudes. For U_{10} it is clear that both RAD and ALT overestimate the wind speed for latitudes greater than 50°N, with RAD overestimating by approximately 3% and ALT by approximately 7%. In contrast, and consistent with the cases shown in Fig. (8), there is no statistically significant effect for H_s.

In Fig. 9 it is also apparent that there is an underestimation of U_{10} at the lower latitudes (i.e. < 50°N). This occurs because the results are normalized against the average across all buoys. Therefore, the average of all values in Fig. 9 must be one. If there is an overestimation for latitudes greater than 50°N, there must be a corresponding underestimation at latitudes less than this value.

5. Wave age and atmospheric stability dependence

There are two obvious possible causes for the observed differences between satellite and buoy observations of U_{10}. The first is that the high wavenumber components of the surface wave spectrum are impacted by a quantity other than the wind speed. One possibility is that there is a wave age (U_{10}/C_m) or wave slope (H_s/L_m) dependence, where C_m is the mean wave phase speed and L_m is the mean wave length. These two quantities are largely indistinguishable as H_s is related to U_{10} and L_m is related to C_m. The second possibility is that there is a seasonal and latitudinal variation in atmospheric stability which impacts the apparent wind speed sensed by the respective satellite systems (see Section 3). In order to investigate these potential impacts additional geophysical parameters are required (C_m for wave age dependence and air and water temperatures for atmospheric stability). As these quantities are not available from the satellite measurements, we rely on the ERA-I reanalysis data. As the ERA-I data is available only at 6 hourly intervals, it is not possible to infer values of these quantities at the times of individual satellite measurements (e.g. cannot resolve the diurnal cycle for air temperature). As a result, we will utilize climatological (mean monthly) values in the following analyses. For these two possibilities, we are seeking evidence of a latitudinal dependence and a seasonal dependence at high latitudes. In addition, we seek a process which will impact ALT more than RAD. Finally, it should impact wind speed but not wave height sensed by the satellite systems.

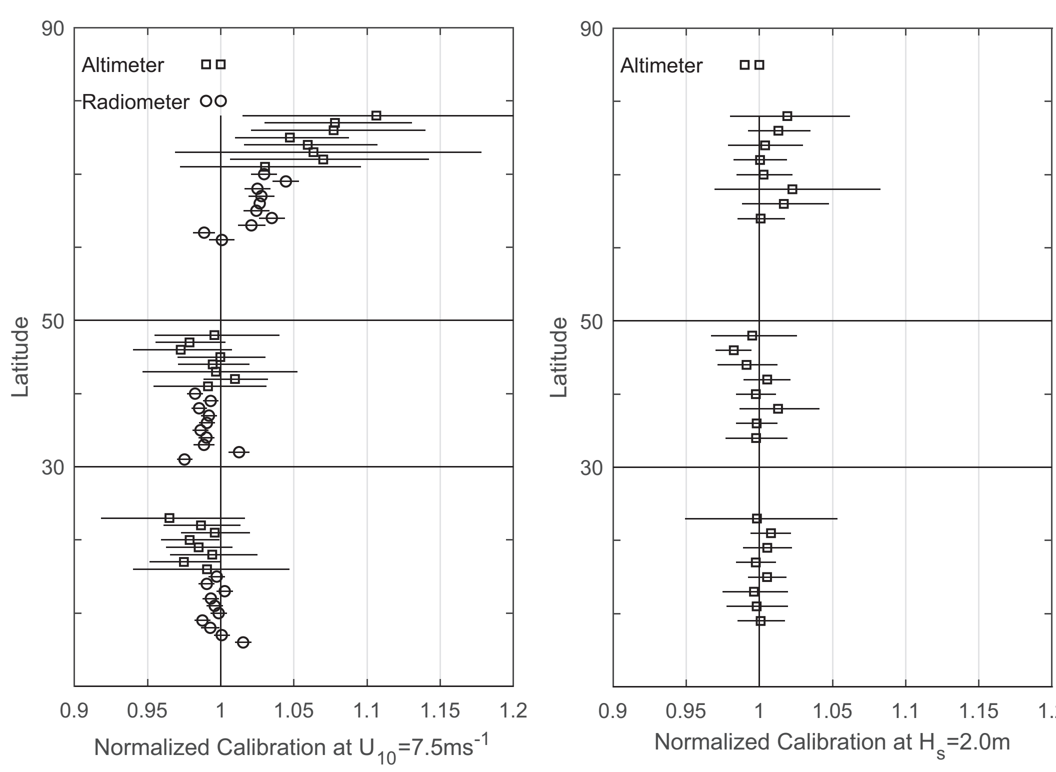

Fig. 9. Normalized regression value for altimeters (□) and radiometers (o). Data is partitioned by latitude: 0° to 30°N, 30°N to 50°N, greater than 50°N. Each data point represents a single satellite mission and values have been stacked vertically for clarity. Values greater than 1 indicate measured quantity larger than the overall mean. U_{10} (left panel), H_s (right panel). Horizonal bars represent 95% confidence intervals.

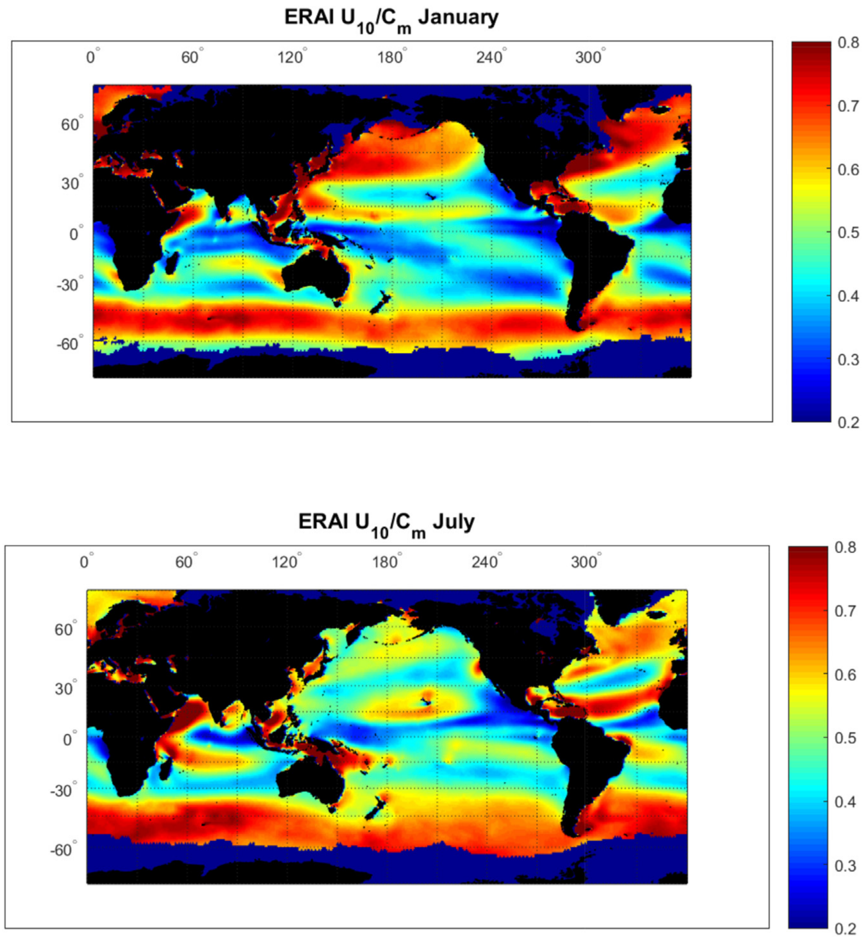

Fig. 10. The wave age, U_{10}/C_m obtained from ERA-I reanalysis data. The plots show mean monthly values: January (top), July (bottom).

5.1. Wave age dependence

As the wave spectrum ages, the peak moves to lower frequencies – higher phase speeds – and longer waves contribute to mss and dissipation. At the same time the shorter waves in the equilibrium range become less steep [Donelan, 2017]. The net effect is that there is virtually no change in dissipation or mss with wave age (fetch) at a given wind speed [Donelan, 2018]; nor is there any significant change in the effective wind speed heights to be expected. Therefore, it is reasonable to assume that the observed latitudinal and seasonal response of the instruments is not significantly related to changes in wave age.

In order to investigate any potential impact of wave age, mean monthly values of wave age U_{10}/C_m were calculated from the ERA-I data. Note that we use, C_m, the mean wave phase speed, rather than the more conventional, C_p, peak wave phase speed, as C_p tends to be a very "noisy" quantity. Fig. 10 shows global values of U_{10}/C_m for the months of January and July.

High values of U_{10}/C_m are associated with actively wind generated seas, whereas low values correspond to swell dominated situations. The data does show a latitudinal dependence in wave age, with the equatorial regions being dominated by swell and the higher latitudes showing waves more dominated by active generation by the local wind.

There is also a seasonal dependence in the northern hemisphere, with higher values of U_{10}/C_m in winter than in summer. However, the southern hemisphere is quite different, with high latitudes showing high values of U_{10}/C_m year-round with little seasonal dependence. Although the available data does not provide buoy comparisons for the southern hemisphere, the differences between ALT and RAD U_{10} [Fig. (6)] suggests similar behaviour to the northern hemisphere. Although we cannot rule out wave age dependence completely, the southern hemisphere behaviour, together with the fact that neither dissipation nor mss are significantly impacted by this quantity make it unlikely that the observed differences in satellite performance are the result of a wave age dependence.

5.2. Atmospheric stability

The key parameter in determining the impact of atmospheric stability is the air-water temperature difference. This quantity determines the bulk Richardson number, Eq. (3) and hence the boundary layer Eq. (1). Based on the ERA-I data, mean monthly values of $\Delta T = T_2 - T_s$ were determined, where T_2 is the air temperature at a height of 2 m and T_s the sea surface temperature (both quantities available in the ERA-I database at 6 hourly intervals). Fig. (11) shows the global distribution of ΔT for the months of January and July. Negative values in Fig. (11) correspond to unstable atmospheric boundary layer conditions (i.e. sea surface temperature greater than air temperature). The striking feature of the figure is that the vast majority of the global oceans are characterised by unstable atmospheric boundary layer conditions, throughout the year. In fact, the only locations where there are regions of significant stable conditions are at high latitudes ($\pm 45^{\circ}$) during summer. The figure does show both a latitudinal dependence as well as a seasonal dependence at high latitudes. Both of these features are consistent with the observed behaviour of the satellite derived wind speeds.

The ERA-I data provides the basis to determine the approximate magnitude of the impact of the atmospheric stability on the observed satellite wind speeds. We have undertaken calculations assuming the

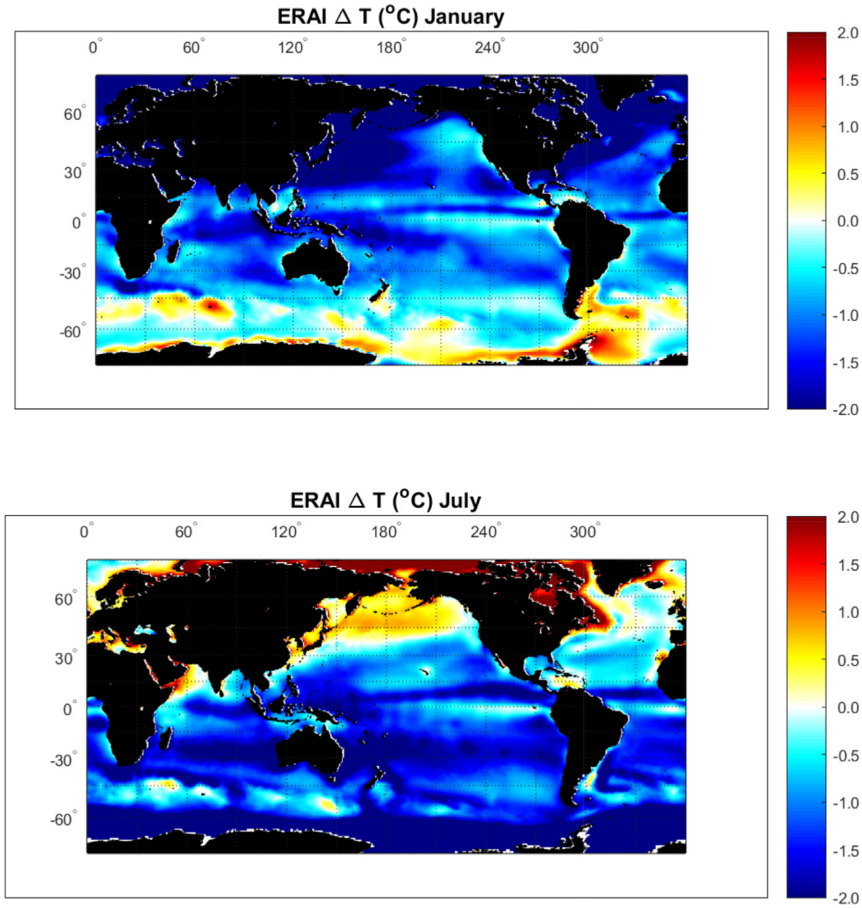

Fig. 11. The air – water temperature difference, $\Delta T = T_2 - T_s$ obtained from ERA-I reanalysis data. Negative values indicate an unstable atmospheric boundary layer. The plots show mean monthly values: January (top), July (bottom).

average sensing height of the satellite wind speed is governed by (a) dissipation and (b) mean squared slope. For each of these cases, it is possible to determine the effective sensing height, z_{sat} using a "look up" table associated with the data shown in Fig. (3). With z_{sat} specified and the air-water temperature difference, ΔT known from the ERA-I climatology, the boundary layer can be determined for the cases of both 'dissipation' and 'mean squared slope' dependence from Eq. (1). These values can be calculated for all points on the global 0.75° × 0.75° ERA-I grid. Consistent with our climatological approach, mean monthly values have been used. Fig. (12) shows the seasonal distribution of a number of quantities at two locations – 57°N, 180°E and 0°, 180°E. That is, a high latitude location and an equatorial location. The quantities shown in the figure are: the air – water temperature difference, ΔT (negative values unstable), $U_{10}(\text{bl})/U_{10}(\text{neutral})$ where $U_{10}(\text{bl})$ is the wind speed calculated from Eq. (1) for the given ΔT and $U_{10}(\text{neutral})$ is the wind speed calculated assuming a neutral boundary layer, $\Delta U_{10} = U_{10}(\text{bl}) - U_{10}(\text{neutral})$ and z_{sat} the effective sensing height of the satellite wind speed. Values are calculated for both the 'dissipation' and 'mss' dependence assumptions.

The air – water temperature difference, ΔT [Fig. (12a) and (e)] shows a strong seasonal cycle for the high latitude case and no seasonal cycle at the equator. The ratio of $U_{10}(\text{bl})/U_{10}(\text{neutral})$ [Fig. (12b) and (f)] shows a strong seasonal signal for the 'mss' result and a weaker signal for the 'dissipation' for the high latitude case and again no seasonal signal at the equator. This is consistent with the buoy – satellite comparisons in Figs. (7) and (9). The result in Fig. (12b) indicates an enhancement of the wind speed of approximately 5% for the 'mss' case, which is in good agreement with the ALT "overprediction" of 7% in Fig. (9). Fig. (12b) indicates an enhancement of only 1% for the 'dissipation' case which again is consistent with the 2% overestimation of RAD in Fig. (9). Note that in Figs. (7) and (9) we averaged the data into three latitude bands to obtain sufficient satellite-buoy "matchups" to yield statistically stable values. This is not necessary for the model output and hence, Fig. (12) shows typical data at two representative locations.

The reason for the much larger seasonal cycle in the 'mss' case is clearly shown in Fig. (12c), which shows that z_{sat} varies between 8 m (winter) and 3 m (summer) for the 'dissipation' case and 2 m (winter) and 0.5 m (summer) for the 'mss' case. The much lower values of z_{sat} associated with the 'mss' case explains why there is a much greater impact from the changes in atmospheric boundary layer structure throughout the year compared to the 'dissipation' case. Fig. (12d) shows ΔU_{10} as a function of month for both the 'dissipation' and 'mss' cases. This result is directly comparable with the buoy-satellite difference plots shown in Fig. (7). Again, the seasonal cycles agree qualitatively, with an overestimation of the wind speed in winter. The ERA-I boundary layer calculations indicate an overestimation of approximately 0.5 ms^{-1} for the 'mss' case and 0.1 ms^{-1} for the 'dissipation' case. This compares to the ALT overestimation of approximately 1 ms^{-1} and RAD overestimation of 0.4 ms^{-1}. Although there are some differences in the magnitude of the wind speed enhancement, the present calculations reproduce surprisingly well the observed qualitative results. This is particularly the case when it is considered that climatological mean values have been used. One would expect such an approach to underestimate the peaks, as seen in the present analysis (see Section 6).

The satellite data indicated that the ALT measured higher winds than the RAD in both summer and winter at high latitudes in both hemispheres [Fig. (6)]. Fig. (13) shows the differences between the

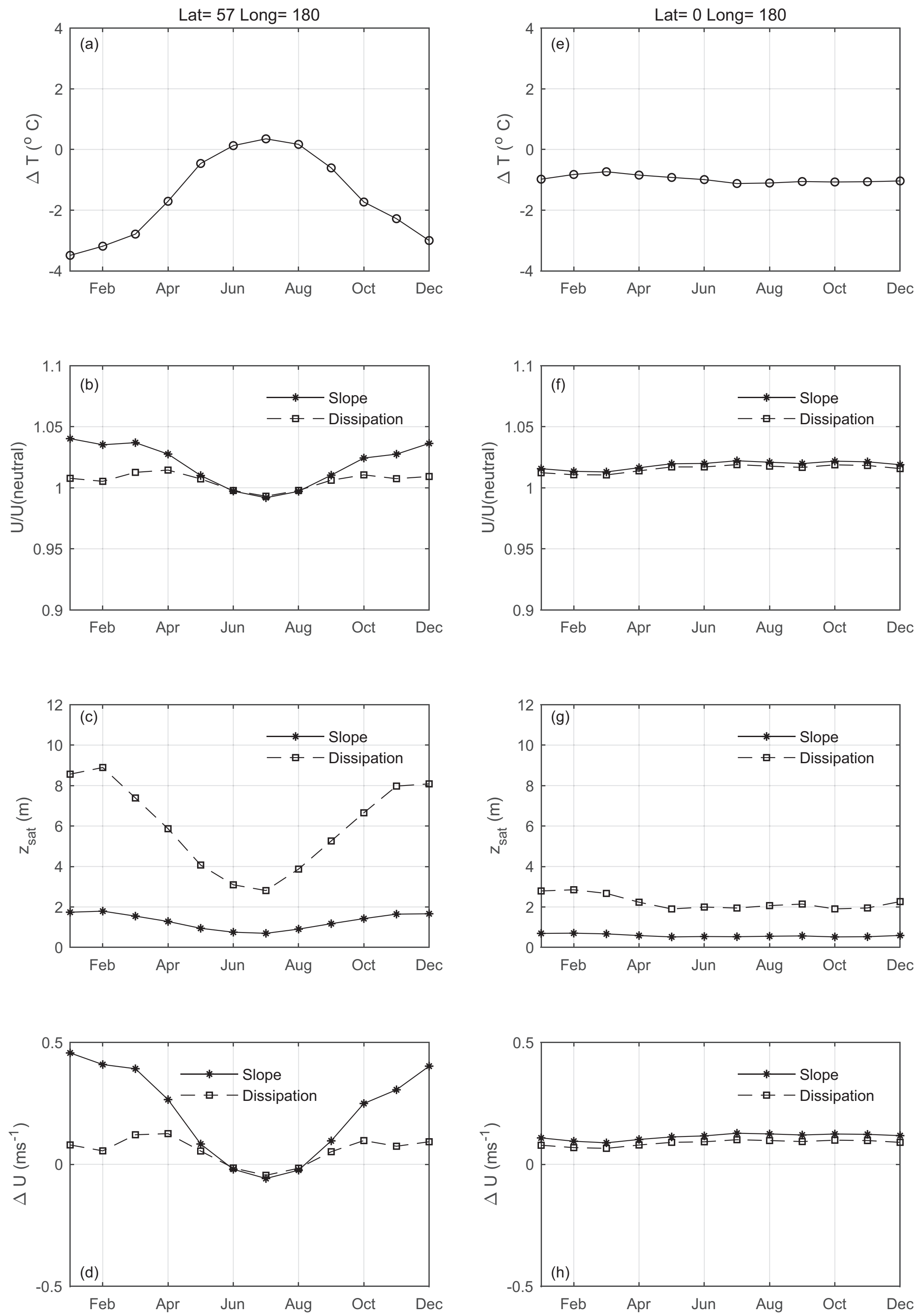

Fig. 12. Seasonal distribution of ERA-I quantities at 57°N, 180°E (left panels) and 0°, 180°E (right panels). Quantities shown are: (a), (e) air – water temperature difference, ΔT (negative values unstable); (b), (f) $U_{10}(\text{bl})/U_{10}(\text{neutral})$ where $U_{10}(\text{bl})$ is the wind speed calculated from Eq. (1) for the given ΔT and $U_{10}(\text{neutral})$ is the wind speed calculated assuming a neutral boundary layer, (c), (g) z_{sat} the effective sensing height of the satellite wind speed and (d), (h) $\Delta U_{10} = U_{10}(\text{bl}) - U_{10}(\text{neutral})$. Values are calculated for both the 'dissipation' and 'mss' dependence assumptions.

'mss' and 'dissipation' calculations with the ERA-I climatological data. This figure can be compared to Fig. (6) for the satellite data. Although the ERA-I calculations indicate that the 'mss' (ALT) result is larger than the 'dissipation' (RAD) in winter, the two calculations are very similar in summer. This can also be seen in Fig. (12d). Hence, we have not been able to reproduce the high latitude summer differences.

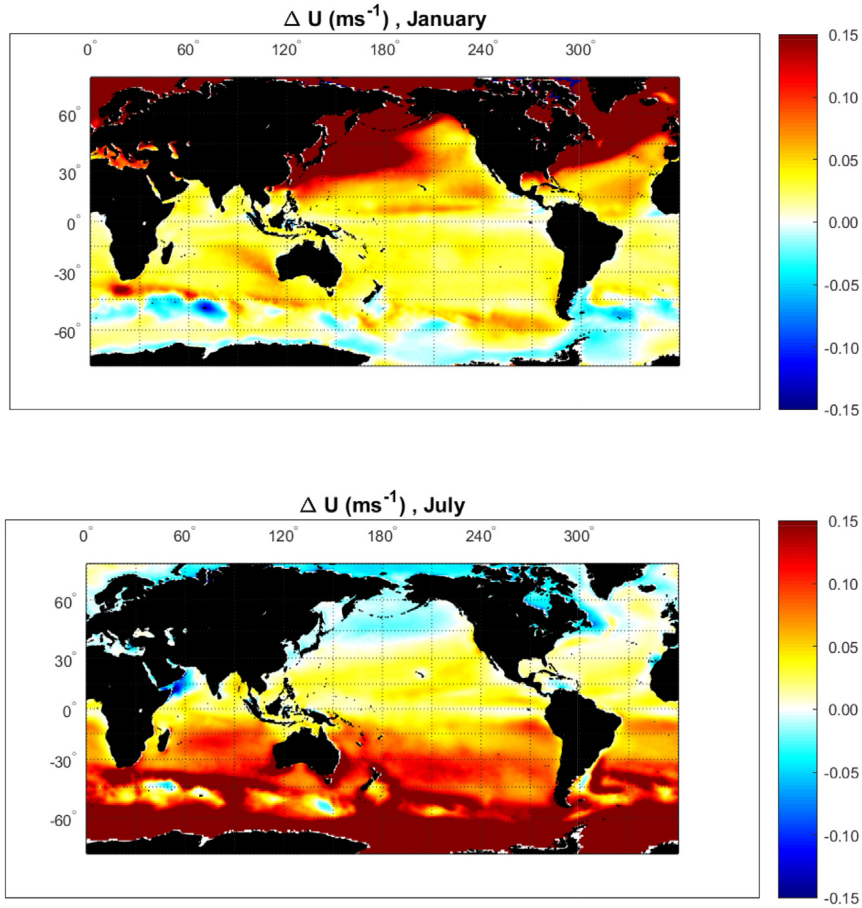

Fig. 13. Difference between wind speed calculated assuming 'mss' and 'dissipation' effective height scaling and a boundary layer as in Eq. (1), $\Delta U_{10} = U_{10}(\text{mss}) - U_{10}(\text{dissipation})$. Positive values represent higher wind speeds with 'mss' height scaling.

6. Discussion

The above analysis, which determines the effective height of the wind speed sensed by ALT and RAD based on the assumptions that they respond to 'mss' and 'dissipation' respectively, explains most of the observed differences in the global distributions of wind speed between these instruments. However, there are still some features not fully explained by the analysis. In particular, the magnitudes of the seasonal variations in wind speed are approximately 60% of those observed. In addition, the satellite data indicates that altimeter wind speeds are higher than radiometer at high latitudes in both summer and winter [see Fig. (6)]. However, calculations based on ERA-I climatology indicate this occurs only in winter [see Figs. (12d), (13)].

A possible explanation for these differences is that the two satellite systems do not, on average, measure winds at the same local times. Therefore, if there is a diurnal variation in wind speed (which is commonly the case with weaker winds at night) this may introduce a bias in the satellite derived winds. Fig. (6), for instance calculates monthly mean values of all satellite observations in each $2^\circ \times 2^\circ$ grid square, irrespective of the time of the observation. As shown in Fig. (1), the distribution of observations throughout the day is quite different between ALT and RAD.

Time of observation issues can be removed by considering only data associated with satellite matchups. That is, data recorded when the ALT and RAD measured at the same time and location. As for the buoy observations, the matchup criteria were set at a spatial separation of 50 km and temporal separation of 30 min. As shown in Fig. (1) the vast bulk of the satellite data will not satisfy these criteria as the local times of observation differ. However, the datasets are large and provided data

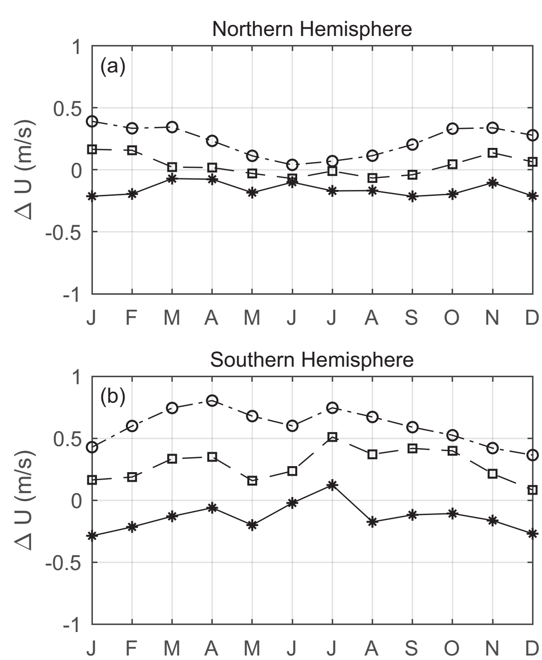

Fig. 14. Wind speed difference $\Delta U = U_{10}(\text{Alt}) - U_{10}(\text{Rad})$ obtained from matchup observations of satellites. The data is partitioned by latitude: 0° to 30°N – (*), 30°N to 50°N – (□), greater than 50°N – (o). Northern Hemisphere data shown in panel (a) and Southern Hemisphere data in panel (b).

is pooled from a number of different missions, a reasonably large global dataset of coincident RAD-ALT measurements can be assembled. The database was searched for matchups between the following satellite combinations: ENVISAT – SSMIf15, GFO – SSMIf15, GFO – SSMIf16, JASON1 – SSMIf13 and TOPEX – SSMIf14. A total of approximately 1.3×10^6 global observations were obtained from these combinations of satellite missions. This data was then partitioned by latitude (0° to 30°, 30° to 50°, 50° to 90°) in a similar manner to the buoy – satellite observations. In this case, however, as we have global data, this process was carried out for both Northern and Southern hemispheres. Fig. (14) shows the values of mean monthly $\Delta U = U_{10}(\text{Alt}) - U_{10}(\text{Rad})$ for each of these latitude bands.

The results show the same general features observed previously. There is little seasonal variation in the differences between the satellites at low latitudes. However, at higher latitudes, the ALT measures higher values of U_{10} than the RAD and there is a strong seasonal variation with the largest differences being seen in winter in both hemispheres. This behaviour is consistent with the predictions from the present analysis [see Fig. (12d)]. However, the results in Fig. 14 differ from the satellite differences averaged over grid squares shown in Fig. (6). Fig. (6) indicates similar differences in ΔU at high latitudes between summer and winter. Therefore, it appears that this is a result of the different local sampling times of ALT and RAD. When this issue is removed by using matchup data, the satellite differences show the same seasonal variations as the calculations [compare Figs. (14) and (12)].

The results in Fig. (14) show little difference between ALT and RAD winds at high Northern latitudes in summer, as predicted in Figs. (12d) and (13) (for July). This occurs because there is only a small air-water temperature differences at high latitudes in the Northern Hemisphere summer [see Fig. (11) (July)]. At high latitudes in the Southern Hemisphere there is again a seasonal variation in the wind speed differences, with the highest differences [$U_{10}(\text{Alt}) > U_{10}(\text{Rad})$] again occurring in winter. However, in contrast to the Northern hemisphere, the ALT predicts higher wind speeds year-round. This is again consistent with the present analysis, as seen in Fig. (13) which shows $U_{10}(\text{Alt}) > U_{10}(\text{Rad})$, year-round. Although the differences decrease in summer, the boundary layer remains unstable throughout the year in the Southern Ocean [see Fig. (11) (January)] and hence the ALT records higher wind speeds.

The observed differences in Fig. (14) have maximum values of approximately 0.5 to 0.6 ms^{-1}. This is consistent with Fig. (12d), indicating the present calculations reproduce not only the latitudinal and seasonal variations but also the approximate magnitudes. Considering that we use climatological monthly mean air-water temperature differences, the comparisons between the observations and predictions are remarkably good.

The approach described in this paper provides the basis for correcting altimeter and radiometer wind speed observations to account for differences in atmospheric stability. This approach was used to calculate the correction factor, $U_{10}/U_{10}(\text{neutral})$ as in Fig. (12b, f). That is, a correction factor for U_{10} satellite observations which is a function of U_{10} [as this specifies the effective sensing height, as in Fig. (3)] and the air-water temperature difference, ΔT (as this changes the boundary layer shape). Fig. (15) shows values of the correction factors for both ALT and RAD as a function of U_{10} and ΔT.

As expected, the corrections are largest at low wind speeds, as the effective sensing height is low for these values. Similarly, the correction factors are larger than one for negative ΔT (unstable conditions) and smaller than one for positive ΔT (stable conditions). In both cases, there is a horizontal contour of value one. This occurs at approximately $U_{10} = 15\,\text{ms}^{-1}$ for the RAD and $U_{10} = 27\text{ms}^{-1}$ for ALT. This line corresponds to the point where the effective sensing height $z_{sat} = 10$ m. Above this line, the correction factor changes from greater than one to less than one (or vice versa). A MATLAB look up table which uses the data in this figure is provided in the Supplementary material.

The present analysis assumes that the ALT responds predominately to mean squared slope and the RAD responds predominately to dissipation. There are sound theoretical bases for these assumptions and the remarkably good agreement between the present observations and the calculations further support these assumptions. Nevertheless, it is possible that the instruments may also be influenced by other quantities (e.g. Radiometer may be impacted by mss in addition to dissipation). However, the present results provide strong support for the hypothesis that these two quantities are the primary quantities sensed by these satellite systems.

The present results show that atmospheric stability effects can impact satellite wind speed measurements by up to 5%. Fetch limited wave growth studies have previously indicated that atmospheric stability can also impact wave growth (Young, 1998), as it changes $U_{\lambda/2}$. However, the present analysis detected no apparent impact on altimeter measurements of H_s, which are essentially radar range measurements.

7. Conclusions

The present study has undertaken an analysis of a very extensive satellite database of approximately 30 years of altimeter and radiometer measurements of wind speed and wave height. This dataset is analysed to provide detailed descriptions of global wind and wave climate which are compared with each other and ERA-I model reanalysis data.

Despite the fact that the datasets have been carefully and consistently calibrated, they show systematic variations in wind speeds as a function of latitude and season. Compared to buoy data, both altimeter

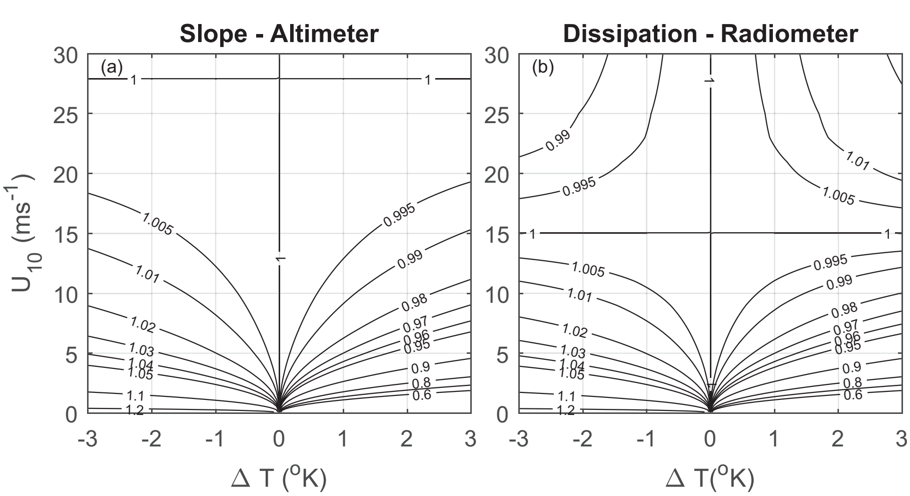

Fig. 15. Correction factors for atmospheric stability for (a) Altimeter and (b) Radiometer.

and radiometer over-estimate wind speed at high latitude during winter. Altimeter derived wind speeds are more impacted than radiometer winds.

The present analysis shows that this is caused by changes in atmospheric stability. As both instruments respond to effective wind speeds relatively close to the water surface, they are impacted by the shape of the boundary layer in inferring wind speeds at an elevation of 10 m from the satellite observations. The observed differences in wind speed are consistent with the mean squared slope being the primary quantity sensed by the altimeter and dissipation being the primary quantity sensed by the radiometer. The analysis is able to reproduce both the variation in wind speeds as a function of latitude and throughout the year. In addition, slightly different behaviour in the two hemispheres is consistent with the observed differences in air-water temperature difference and is quantitatively explained by the present analysis.

The importance of considering the time of day of satellite wind speed observations is also highlighted by the analysis. As wind speed generally exhibits a diurnal variation, instruments which preferentially measure at defined times of day will bias results. As ALT and RAD systems measure at different local times, long term statistics will exhibit differences between these instruments for this reason.

Acknowledgements

This work was financially supported by the Australian Research Council (ARC) through Discovery Grants DP130100215 and DP160100738. This support has been invaluable in completing this extensive study. The raw datasets used in the study were supplied by *Globwave* (altimeter and buoy) and *Remote Sensing Systems* (RSS) (radiometer/scatterometer). Without these public domain archives, the study would have been extremely difficult.

Mark Donelan tragically passed away on 12 March 2018, less than 2 weeks after this paper was submitted for review. As such, it represents the last published contribution from a remarkable scientist.

Appendix A. Supplementary data

Supplementary data to this article can be found online at https://doi.org/10.1016/j.rse.2018.06.006.

References

Abdalla, S., 2007. Ku-band radar altimeter surface wind speed algorithm. In: Envisat Symposium 2007. European Centre for Medium-Range Weather Forecasts, UK.

Arya, S.P., 1988. Introduction to Meteorology. Academic Press, San Diego (307 pp.).

Businger, J.A., Wyngaard, J.C., Izumi, I., Bradley, E.F., 1971. Flux-profile relationships in the atmospheric surface layer. J. Atmos. Sci. 28, 181–189.

Chelton, D.B., Ries, J.C., Haines, B.J., Fu, L.-L., Callahan, P.S., 2001. Satellite Altimetry, Satellite Altimetry and Earth Sciences: A Handbook of Techniques and Applications. Academic Press, pp. 1–131 (chap. 1).

Cheney, R.E., Douglas, B.C., Agreen, R.W., Miller, L., Porter, D.L., Doyle, N., 1987. GEOSAT Altimeter Geophysical Data Record: User Handbook. NOAA, Rockville.

Cotton, P.D., Carter, D.J.T., 1994. Cross calibration of TOPEX, ERS-1, and Geosat wave heights. J. Geophys. Res. 99 (12). http://dx.doi.org/10.1029/94JC02131. (25 025–25 033).

Cox, C.S., Munk, W.H., 1954. Measurements of the roughness of the sea surface from photographs of the sun's glitter. J. Opt. Soc. Am. 44 (838–850), 340.

Dee, D.P., et al., 2011. The ERA-Interim reanalysis: configuration and performance of the data assimilation system. Q. Jnl. Roy. Met. Soc. 137, 553–597.

Donelan, M.A., 2017. Frequency-direction spectra of wind-generated gravity waves. In: Encyclopedia of Maritime and Offshore Engineering. John Wiley & Sons. http://dx.doi.org/10.1002/9781118476406.emoe079.

Donelan, M.A., 2018. On the decrease of the oceanic drag coefficient in high winds. J. Geophys. Res. Oceans 123. http://dx.doi.org/10.1002/2017JC013394.

Donelan, M.A., Curcic, M., Chen, S.S., Magnusson, A.K., 2012. Modeling waves and wind stress. J. Geophys. Res. 117. http://dx.doi.org/10.1029/2011JC007787.

Dyer, A.J., Hicks, B.B., 1970. Flux-gradient relationships in the constant flux layer. Q. J. R. Meteorol. Soc. 96, 715–721.

Holthuijsen, L.H., 2007. Waves in Oceanic and Coastal Waters. Cambridge University Press (387 pp.).

Hwang, P.A., 2012. Foam and roughness effects on passive microwave remote sensing of the ocean. IEEE Trans. Geosci. Remote Sens. 50 (8), 2978–2985.

Hwang, P.A., Fois, F., 2015. Surface roughness and breaking wave properties retrieved from polarimetric microwave radar backscattering. J. Geophys. Res. 120, 3640–3657.

Hwang, P.A., Teague, W.J., Jacobs, G.A., Wang, D.W., 1998. A statistical comparison of wind speed, wave height and wave period derived from satellite altimeters and ocean buoys in the Gulf of Mexico Region. J. Geophys. Res. 103, 10451–10468.

Janssen, P.A.E.M., 2008. Progress in ocean wave forecasting. J. Comput. Phys. 227, 572–3594.

Johnson, J.T., Zhang, M., 1999. Theoretical study of the small slope approximation for ocean polarimetric thermal emission. IEEE Trans. Geosci. Remote Sens. 37, 2305–2316.

Kahma, K.K., Calkoen, C.J., 1992. Reconciling discrepancies in the observed growth of wind-generated waves. J. Phys. Oceanogr. 22, 1389–1405.

Komen, G.J., Cavaleri, L., Donelan, M., Hasselmann, K., Hasselmann, S., Janssen, P.A.E.M., 1994. Dynamics and Modelling of Ocean Waves. Cambridge Univ. Press (532 pp.).

Kumar, A., Zhang, L., Wang, W., 2013. Sea surface temperature–precipitation relationship in different reanalyses. Mon. Weather Rev. 141, 1118–1123.

Lumley, J.L., Panofsky, H.A., 1964. The Structure of Atmospheric Turbulence. Interscience.

Meissner, T., Wentz, F., Ricciardulli, L., 2014. The emission and scattering of L-band microwave radiation from rough ocean surfaces and wind speed measurements from the Aquarius sensor. J. Geophys. Res. Oceans 119, 6499–6522. http://dx.doi.org/10.1002/2014JC009837.

Meissner, T., Wentz, F., Ricciardulli, L., 2017. Capability of the SMAP mission to measure ocean surface winds in storms. Bull. Am. Meteorol. Soc. 98, 1660–1677.

Monin, A.S., Obukhov, A.M., 1954. Basic relationships of turbulent mixing in the surface layer of the atmosphere. Akad. Nauk. SSSR Trud. Geofiz. Inst. 24 (151), 163–187.

Monin, A.S., Yaglom, A.M., 1971. Statistical Fluid Mechanics. MIT Press (769 pp.).

Munk, W., 2009. An inconvenient sea truth: spread, steepness, and skewness of surface slopes. Annu. Rev. Mar. Sci. 1, 377–415. http://dx.doi.org/10.1146/annurev.marine.010908.163940.

Plant, W.J., 2002. A stochastic, multiscale model of microwave backscatter from the ocean. J. Geophys. Res. 107, C93120. http://dx.doi.org/10.1029/2001JC000909.

Priestly, C.H.B., 1959. Turbulent Transfer in the Lower Atmosphere. Univ. Chicago Press.

Queffeulou, P., 2004. Long-term validation of wave height measurements from altimeters. Mar. Geod. 27, 495–510. http://dx.doi.org/10.1080/01490410490883478.

Stogryn, A., 1972. The emissivity of sea foam at microwave frequencies. J. Geophys. Res. 77, 1650–1666.

Walker, D.M., 1995. Measurement techniques and capabilities of the Geosat Follow-On (GFO) radar altimeter. In: 2nd Topical Symposium on Combined Optical-Microwave Earth and Atmosphere Sensing, pp. 226–228. http://dx.doi.org/10.1109/COMEAS.1995.472314.

Webb, E.K., 1970. Profile relationships: the log-linear range, and extension to strong stability. Q. J. R. Meteorol. Soc. 96, 67–90.

Wentz, F.J., 1983. A model function for ocean microwave brightness temperatures. J. Geophys. Res. 88, 1892–1908.

Wentz, F.J., 1992. Measurement of oceanic wind vector using satellite microwave radiometers. IEEE Trans. Geosci. Remote Sens. 30, 960–972.

Wentz, F.J., 1997. A well-calibrated ocean algorithm for special sensor microwave/imager. J. Geophys. Res. 102 (C4), 8703–8718.

Yang, D., Meneveau, C., Shen, L., 2013. Dynamic modelling of sea-surface roughness for large-eddy simulation of wind over ocean wave-field. J. Fluid Mech. 726, 62–99.

Young, I.R., 1993. An estimate of the Geosat altimeter wind speed algorithm at high wind speeds. J. Geophys. Res. 98 (C11), 20,275–20,285.

Young, I.R., 1994. Global Ocean wave statistics obtained from satellite observations. Appl. Ocean Res. 16, 235–248.

Young, I.R., 1998. Experimental investigation of the role of atmospheric stability in wind wave growth. Coast. Eng. 34, 23–33.

Young, I.R., 1999a. An intercomparison of GEOSAT, TOPEX and ERS1 measurements of wind speed and wave height. Ocean Eng. 26, 67–81.

Young, I.R., 1999b. Seasonal variability of the global ocean wind and wave climate. Int. J. Climatol. 19, 931–950.

Young, I.R., Holland, G.J., 1996. Atlas of the Oceans: Wind and Wave Climate. Pergamon Press (ISBN 0-08-042519-4, 241 pp.).

Young, I.R., Sanina, E., Babanin, A.V., 2017. Calibration and cross-validation of a global wind and wave database of Altimeter, Radiometer and Scatterometer measurements. J. Atmos. Ocean. Technol. 1285–1306. http://dx.doi.org/10.1175/JTECH-D-16-0145.1.

Yueh, S.H., Kwok, R., Li, F.K., Nghiem, S.V., Wilson, W.J., Kong, J.A., 1994. Polarimetric passive remote sensing of ocean wind vectors. Radio Sci. 29, 799–814.

Zieger, S., Vinoth, J., Young, I.R., 2009. Joint calibration of multi-platform altimeter measurements of wind speed and wave height over the past 20 years. J. Atmos. Ocean. Technol. 26 (12), 2549–2564. http://dx.doi.org/10.1175/2009JTECHA1303.1.